Underwater blast response of free-standing sandwich plates with metallic lattice cores

G.J. Mcshane, V.S. Deshpande, N.A. Fleck

To cite this version:

G.J. Mcshane, V.S. Deshpande, N.A. Fleck. Underwater blast response of free-standing sandwich plates with metallic lattice cores. International Journal of Impact Engineering, 2010, 37 (11), pp.1138. ⟨10.1016/j.ijimpeng.2010.05.004⟩. ⟨hal-00723002⟩

HAL Id: hal-00723002
https://hal.science/hal-00723002v1

Submitted on 7 Aug 2012

Accepted Manuscript

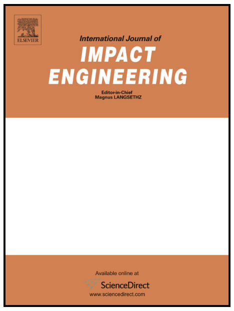

International Journal of

IMPACT ENGINEERING

Editor-in-Chief

Magnus LANGSETH

Available online at

ScienceDirect

www.sciencedirect.com

Title: Underwater blast response of free-standing sandwich plates with metallic lattice cores

Authors: G.J. McShane, V.S. Deshpande, N.A. Fleck

PII: S0734-743X(10)00094-1

DOI: 10.1016/j.ijimpeng.2010.05.004

Reference: IE 1893

To appear in: *International Journal of Impact Engineering*

Received Date: 21 April 2009

Revised Date: 19 May 2010

Accepted Date: 29 May 2010

Please cite this article as: McShane GJ, Deshpande VS, Fleck NA. Underwater blast response of free-standing sandwich plates with metallic lattice cores, International Journal of Impact Engineering (2010), doi: 10.1016/j.ijimpeng.2010.05.004

Underwater blast response of free-standing sandwich plates with metallic lattice cores

G.J. McShane, V.S. Deshpande, N.A. Fleck

Department of Engineering, University of Cambridge

Trumpington Street Cambridge, CB2 1PZ, UK.

Abstract

The underwater blast response of free standing sandwich plates with a square honeycomb core and a corrugated core has been measured. The total momentum imparted to the sandwich plate and the degree of core compaction are measured as a function of (i) core strength, (ii) mass of the front face sheet (that is, the wet face) and (iii) time constant of the blast pulse. Finite element calculations are performed in order to analyse the phases of fluid-structure interaction. The choice of core topology has a strong influence upon the dynamic compressive strength and upon the degree of core compression, but has only a minor effect upon the total momentum imparted to the sandwich. For both topologies, a reduction in the mass of the front (wet) face reduces the imparted momentum, but at the expense of increased core compression. Conversely, an increase in the time constant of the blast pulse results in lower core compression, but the performance advantage over a monolithic plate in terms of imparted momentum is reduced. The sandwich panel results are compared with analytical results for monolithic plates of mass equal to that of (i) the sandwich panel and (ii) the front face alone. (Case (i) represents a rigid core while (ii) represents a core of negligible strength.) For most conditions considered, the sandwich results lie between these limits reflecting the coupled nature of core deformation and fluid-structure interaction.

Keywords: sandwich structures, lattice materials, underwater blast, fluid-structure interaction.

1. Introduction

Shock mitigation is an important consideration in the design of military and commercial vehicles: submersed structures may be subjected to an underwater explosion. Recently, attention has been paid to the potential use of sandwich plates in this protective role. Fleck and Deshpande [1] and Xue and Hutchinson [2] have argued that an underwater blast imparts a lower momentum to sandwich plates than monolithic plates of equal mass. The reduced momentum is associated with the earlier onset of cavitation in the water for sandwich plates with a light front face sheet and a deformable core. Fully coupled finite element calculations of the underwater blast response of sandwich structures support these predictions [3-6]. The degree of fluid-structure interaction (FSI), and consequently the benefits offered by sandwich construction, depends upon the dynamic compressive response of the core, core thickness, span of structure between supports, and the boundary conditions on the plate.

The parametric studies of Liang et al. [5] and Tilbrook et al. [7] reveal that reduced reaction forces at the supports and reduced deflections of the dry, distal face of the structure are achieved through the use of a weak core and a large ratio of core thickness to span. However, the optimal choice of core depends upon the intensity of the applied loading. At large incident blast impulses, an increased thickness or strength of core is required to prevent core densification and ‘slapping’ of the face sheets.

Lattice structures such as corrugations, honeycombs and trusses have high quasi-static stiffness and strength [8-9] and high dynamic strength [10-11]: they show potential as the cores of sandwich plates. However, experimental studies are needed in order to demonstrate explicitly their performance advantage in terms of underwater blast resistance.

There have been recent advances in experimental methods for probing the response of structures to water blast. For example, Wei et al. [12] and Wadley et al. [13] have used sheet explosive to generate a planar blast pulse in water which impinges upon free standing sandwich plates with metallic lattice cores. The sandwich plate was supported on its back face (dry face) and the imparted impulse was measured at the back face supports. These studies reveal that the imparted impulse for the sandwich plate with a deformable core is less than that for a monolithic plate. It remains to show that a reduced impulse is imparted for freely supported or edge-clamped sandwich plates.

Deshpande et al. [14] have developed a laboratory-scale underwater blast simulator to replicate the characteristics of underwater blast loading without the experimental complexities associated with explosive tests. The apparatus consists of a steel tube containing a column of water. This is sealed at one end by an aluminium piston and at the other end by a circular sandwich specimen; both ends are free to slide within the tube. To generate the shock pulse, a steel projectile is accelerated by a gas gun and is then impacted against the aluminium piston. Measurements by Deshpande et al. [14] reveal that a planar pressure pulse propagates from the piston into the water column: the pressure p imposed by the piston on the water column varies with time t according to

$$p(t) = p_0 e^{-t/\theta}, \tag{1}$$

where the parameters (p_0, θ) characterise the blast. Time $t = 0$ corresponds to the arrival of the blast (such that $p = 0$ for $t < 0$). This exponential shape is a reasonable approximation to the blast pulse generated by an explosive detonation in water [15-16]. The blast decay constant θ for the shock wave in the shock tube apparatus is given by

$$\theta = \frac{m_p}{\rho_w c_w}, \tag{2}$$

where m_p is the combined mass per unit area of the projectile and piston, ρ_w is the density of water and c_w is the speed of sound in water. The peak pressure p_0 is given by

$$p_0 = \rho_w c_w v_p, \tag{3}$$

where v_p is the initial velocity of the combined projectile and piston mass immediately after impact. Thus, by varying the mass and velocity of the projectile, the peak pressure and decay constant can be independently adjusted. Experimental measurements of the core compression experienced by sandwich plates with aluminium foam cores are presented by Deshpande et al. [14], and agree well with numerical predictions.

Espinosa et al. [17] have also used a shock tube to generate underwater blast pulses. In contrast to the circular cylindrical shock tube of Deshpande et al. [14], Espinosa and co-workers use a conical tube such that the diameter increases towards the target end. Mori et al. [18-19] used this technique to load edge-clamped sandwich panels with metallic lattice cores. The back face of the sandwich plates deflected less than monolithic plates of equal mass. Although the dynamic deformation and failure modes may be determined by this method, the imparted impulse was not measured directly. However, it is likely that the sandwich plate acquires a smaller impulse than the monolithic plate of equal mass, due to fluid-structure interaction effects.

1.1 Overview of fluid-structure interaction

Taylor [20] considered the one dimensional problem of a planar blast pulse in water impinging upon a free-standing planar, rigid plate. The water is treated as an acoustic, cavitating medium with sound speed $c_w = 1400\ \text{ms}^{-1}$, density $\rho_w = 1000\ \text{kgm}^{-3}$ and cavitation pressure $p_{cav} = 0$. A reference value of total blast impulse I_0 is specified by the impulse per unit area that it would impart on a rigid stationary plate

$$I_0 = 2\int_0^\infty p(t)\,dt = 2p_0\theta. \tag{4}$$

(The factor of 2 arises due to full reflection of the shock wave by the stationary plate.) Taylor [20] showed that the impulse I_t transmitted to a rigid plate of areal mass m, and *free to translate*, is given by

$$\frac{I_t}{I_0} = \psi^{\psi/(1-\psi)}, \tag{5}$$

in terms of a single non-dimensional fluid-structure-interaction (FSI) parameter

$$\psi = \frac{\rho_w c_w \theta}{m}. \tag{6}$$

Consider now the case of a free-standing sandwich plate with rigid front and back face sheets of areal mass m_f and m_b, respectively. The deformable core is of areal mass m_c. For later convenience, we introduce two FSI parameters for the sandwich plate, analogous to (6) for the monolithic plate: the parameter

$$\psi_t = \frac{\rho_w c_w \theta}{m_t} \tag{7}$$

is based on the total areal mass of the sandwich plate $m_t = m_f + m_c + m_b$, while

$$\psi_f = \frac{\rho_w c_w \theta}{m_f} \tag{8}$$

is based on the areal mass of the front face sheet. Two limiting behaviours of the sandwich plate can be deduced immediately:

Case (i). If the core strength is sufficiently high that negligible core deformation occurs during the period of fluid-structure interaction, then the sandwich will behave as a monolithic plate, and ψ_t dictates the response [3].

Case (ii). If the sandwich core offers negligible resistance to the motion of the front face sheet throughout the period of fluid-structure interaction, then the imparted momentum can be calculated using the Taylor [20] analysis with $\psi = \psi_f$ [1-2].

In both cases, the transmitted impulse follows directly from (5) upon interpreting ψ as either ψ_f or ψ_t. Since ψ_f always exceeds ψ_t, we deduce that the transmitted impulse for a deformable core is less than that for a rigid core (or for a monolithic plate of areal mass m_t).

1.2 Scope of study

The objective of the present study is to examine by a combination of experiment and finite element modelling the underwater blast loading response of sandwich plates with metallic lattice cores. The scope is restricted to free-standing sandwich plates. The experimental technique of Deshpande et al. [14] is used in order to obtain the total momentum imparted to the sandwich, in addition to measurements of the core deformation. The response is determined as a function of lattice core topology and of the FSI parameters.

It is anticipated that a greater FSI effect is present in the laboratory-sized specimens of the present study compared to that of a full scale sandwich structure in a ship hull, for example. This stems from the fact that the areal masses of the face sheet and of the sandwich plate are much less than those of the full scale plate. Consequently the Taylor parameter ψ is larger in the experimental study. This lack of similitude associated with the scaling effect is not of concern, as the intent of the study is to explore the FSI phenomenon.

The study is organised as follows. In Section 2 the sandwich specimens are described and the quasi-static compressive response is given. In Section 3 the dynamic test procedure is outlined, and in Section 4 experimental results are reported. In Section 5, finite element analysis is used to gain additional insight into the experimental results. Finally, concluding remarks are given in Section 6.

2. Manufacture and quasi-static properties of the sandwich specimens

2.1 Geometry and fabrication of the sandwich specimens

In this study we consider two core topologies: the corrugated core (Figure 1a) and the square honeycomb core (Figure 1b). These have been selected because they provide a contrast in compressive strength, due to differences in the modes of buckling collapse

[21-23]. However, we do not attempt to optimise aspects of the core geometry in the present study.

The sandwich specimens are circular in plan view and of diameter $D = 64$ mm. The fabrication route is detailed in Appendix A. Both types of core were constructed from brazed AISI 304 stainless steel sheet of thickness $a = 0.3$ mm and density $\rho = 7950$ kgm^{-3}. This material has been used in a number of recent experimental and numerical studies of the dynamic compressive response of metallic lattices [21-24]. AISI 304 stainless steel is a ductile steel which, in the brazed condition, has a similar yield strength and strain hardening characteristics to the structural steels used in ship-building, such as Lloyd's Grade A steel [25]. The uniaxial tensile true stress versus logarithmic plastic strain response of the AISI 304 stainless steel sheet in the as-brazed condition was measured at a nominal strain rate of $\dot{\varepsilon} = 10^{-3}$ s^{-1} and is plotted in Figure 2. Additionally, the high-strain-rate tensile response is given in Figure 2, taken from Stout and Follansbee [26]. The following points are considered in the specification of the core geometry. (i) The cell size must be small enough to fit an adequate number of lattice unit cells within the water blast apparatus. (ii) The relative density of the lattices should allow a range of core compression to be achieved with the blast pressures available. The corrugated core consists of stainless steel sheet folded to a corrugation angle $\omega = 60°$ and a core height $h_c = 22$ mm. Each specimen therefore contains four legs (Figure 1a). The relative density of the core is $\bar{\rho} \approx a/\left(h_c \cos\omega\right) = 2.7\%$ The square honeycomb core, consisting of five cells arranged in a cross shape (Figure 1b), is oriented with the prismatic direction normal to the face sheets. The core height is $h_c = 22$ mm (identical to the corrugated core) and the cell size is $l = 17$ mm. The relative density of the square honeycomb $\bar{\rho} \approx 2a/l = 3.5\%$ slightly exceeds that of the corrugated core due to restrictions on the maximum achievable cell size.

The circular face sheets were machined from 6082-T6 aluminium alloy bar of yield strength 285 MPa and density 2710 kgm^{-3}. This strength was adequate to ensure that the face sheets undergo negligible plastic deformation in the shock tube experiments. For these free-standing plate experiments, the choice of material for the face sheets does not influence the results as long as the transit time for elastic stress waves is small with respect to the time-scales of FSI (as is the case here). The faces can be considered effectively rigid. A groove of depth 3.0 mm and width 3.6 mm is cut into the front face sheet to contain a rubber O-ring, and this provides for sealing against the inner wall of the shock tube. The use of aluminium alloy rather than steel for the faces allows a larger face sheet thickness (for a given mass) in which to support this O-ring.

2.2 Quasi-static compressive response

In order to compare the quasi-static out-of-plane compressive response of the two cores, sandwich specimens were fabricated as described in Appendix A. Corrugated and square honeycomb cores were bonded to aluminium alloy face sheets of thickness $h_f = h_b = 8\,\text{mm}$ and diameter $D = 64\text{ mm}$. The circular sandwich assembly slid freely within an aluminium alloy tube of internal diameter 64.2 mm, replicating the lateral constraint imposed in the dynamic tests. The sandwiches were compressed between rigid platens using a screw-driven test machine at a nominal strain rate of $\dot{\varepsilon}_N = 10^{-3}\text{ s}^{-1}$. The nominal compressive strain within the core, ε_N, defined as the reduction in core height Δh_c divided by the original height, $h_c = 22\text{ mm}$, was measured using a laser extensometer. The nominal core strength, σ_N, defined positive in compression, was calculated from the measured axial force.

The compressive response of the square honeycomb core and of the corrugated core are given in Figures 3a and 3b, respectively. Both topologies show an initial peak in strength followed by softening due to buckling of the core members. This softening response differs qualitatively from the post-yield plateau of metallic foams, as observed by Deshpande et al. [14] and as modelled by Deshpande and Fleck [3]. The peak compressive strength of the lattice core is also sensitive to the details of the topology. The peak strength and post-buckling strength of the square honeycomb are both significantly higher than that of the corrugated core. Both cores exhibit a rapid increase in strength as the core densifies at a nominal compressive strain $\varepsilon_N \approx 0.70$ for the square honeycomb and $\varepsilon_N \approx 0.85$ for the corrugated core. The quasi-static responses should only be considered as indicative of the relative behaviour of the two cores under dynamic loading. The dynamic modes of collapse, and the corresponding dynamic core resistance, depend upon the crushing velocity and are sensitive to the topology [21-22, 24, 27]. The dynamic response of the two topologies has been evaluated by finite element simulations, as reported in Section 5.

3. The water blast experiments

3.1 Water blast apparatus

The underwater blast apparatus of Deshpande et al. [14] was employed, as illustrated in Figure 4. A thick-walled steel tube of internal diameter $D = 64\text{ mm}$, external diameter D_0 = 102 mm and length 1500 mm contains the water column. The diameter of the steel tube is larger than that used in [14] in order to accommodate the lattice sandwich cores. The tube is sealed at one end by an aluminium piston of thickness $10\ \text{mm}$ and mass 0.083kg, and at the other end by the circular sandwich specimen, as described in Section 2. Rubber O-rings in the piston and front face sheet of the sandwich provide the necessary water-tight seal. Note that both the piston and sandwich plate are free to slide within the tube. A bleed valve in the piston is used to remove any air from the tube.

The blast pulse decay constant and peak pressure were varied via the mass and velocity of the projectile (which has diameter 50 mm), as described by Deshpande et al. [14] and summarised in Section 1. Predictions for p_0 and θ were obtained using equations (2) and (3), with the velocity of the projectile measured at the exit of the gas gun barrel using a laser velocity gauge. In addition to these predictions, each blast pulse was measured via the hoop strain on the external surface of the steel tube, located $200\ \text{mm}$ from the impacted end. Foil gauges were used in a Wheatstone bridge configuration with a strain bridge amplifier of cut-off frequency 500 kHz. The internal pressure was calculated from the hoop strain measurements $\varepsilon_h(t)$ using the standard result for an elastic thick-walled cylinder of Young's modulus $E = 210$ GPa subjected to internal pressure $p(t)$:

$$p(t) = \left(\frac{D_0^2 - D^2}{2D^2} \right) E \varepsilon_h(t). \tag{9}$$

Deshpande et al. [14] found good agreement between pressure measurements obtained using the external strain gauge approach (9) and a piezoelectric water pressure sensor. Measured values of p_0 and θ are obtained by fitting an exponentially decaying curve, equation (1), to the data. These measured values are assumed when interpreting the experimental results. Peak pressures in the range p_0 = 24 – 114 MPa and decay constants $\theta \approx 0.13\ \text{ms}$ and $0.26\ \text{ms}$ were obtained using steel projectiles of mass 0.5 kg and 1.1 kg, respectively. Predicted value of p_0 and θ agreed with the measured value to within about 5%.

The experimental approach of Deshpande et al. [14] has been modified in order to allow the momentum imparted to the sandwich specimens to be measured. The total momentum imparted to the sandwich panel by the blast wave is found by measuring the terminal velocity of the compressed sandwich plate at the exit of the water tube using a laser velocity gauge (Figure 4). The specimen breaks three laser beams in turn, and the time differences are recorded. The rear face of the sandwich plate is initially located inside the water shock tube, $30\ \text{mm}$ from the free end, in order to allow the fluid-structure interaction to complete before the specimen exits the tube and passes through the velocity gauge. High speed photographs taken at the exit of the apparatus confirm the final velocity of the sandwich and verify that an adequate seal was maintained at the sandwich front face during the experiment. An example is shown in Figure 5 for a square honeycomb core sandwich: note that no water has leaked past the sandwich.

In order to validate the experimental procedure for measuring I_t, a test case was performed. A monolithic aluminium alloy specimen of mass $m_t = 99\ \mathrm{kgm}^{-2}$ was subjected to a water blast and it was found that the measured transmitted momentum was within 2% of the of the Taylor prediction (5).

Previous numerical simulations by Tilbrook et al. [7] revealed that sandwich cores which experience partial compression following blast loading undergo negligible elastic spring back. The maximum and final core compressions are approximately equal. However, if the blast impulse is sufficient to lead to full core densification, the faces slap together and rebound. A technique is needed in these cases to measure the maximum compressive strain of the core. The maximum core compression during the blast event was obtained as follows for the corrugated core specimens. A strip of aluminium foam, of length 40 mm, width 5 mm and thickness 2 mm, was placed within the central corrugation, as shown in Figure 6a. The strip is crushed plastically as the core compresses (Figure 6b), and elastic recovery of the strip is negligible, see Figure 6c. The strip is of sufficiently low crushing strength, volume and mass to have negligible influence upon the deformation response of the core. For the square honeycomb core sandwich structures (whose closed topology did not permit a similar technique), the maximum core compression was evaluated by measuring the permanent change in core height h_c after blast loading. (The finite element calculations described subsequently verify that elastic recovery for this topology is negligible across the full range of blast impulses considered, and the maximum and final (permanent) core compressions are nearly identical.)

3.2 Outline of the experimental study

Two performance metrics will be considered in the assessment of sandwich performance: the total momentum imparted by the water blast and the degree of core compression. The sensitivity of these performance metrics to the values of ψ_t and ψ_f are explored for both types of core. To achieve this, three series of tests were performed, with the value of peak pressure p_0 varied in each series. The masses of the face sheets and cores in each series are listed in Table 1, along with the values of ψ_t, ψ_f and θ.

In test series 1 and 2, the total mass of the sandwich plates was held constant, thereby keeping ψ_t constant. However, the value of ψ_f in series 2 was twice that of series 1, obtained by reducing the mass of the front (wet) face sheet by a factor of 2 (see Table 1). If the parameter ψ_t governs the response, series 1 and 2 should yield similar sandwich plate performances.

In contrast, in test series 2 and 3, ψ_f was held constant while ψ_t was varied by a factor of 2. This was achieved by varying both the front face sheet mass and the time constant θ by a factor of 2. (θ was altered via the projectile mass.) If ψ_f alone determines the response, then the responses in series 2 and 3 will be identical.

4. Experimental results

The results of the underwater blast experiments for the three series of experiments are given in Figure 7. Individual experimental measurements are indicated by square symbols for the square honeycomb core, and triangular symbols for the corrugated core. The variation in maximum nominal core compression ε_C with total blast impulse I_0 is plotted in Figure 7a. ε_C was measured using the techniques described in Section 3.1. The results for I_t / I_0 are collected together in Figure 7b for series 1 and 2, and in Figure 7c for series 2 and 3.

4.1 The influence of core topology

The results for both topologies are compared in Figure 7 and the same trends emerge for the three series of tests. The corrugated core undergoes larger compressions than the square honeycomb, consistent with its lower quasi-static strength. For the corrugated core, significant differences exist between the maximum core compression (Figure 7a) and the final core compression (not shown).

Photographs of as-tested specimens from series 1 are shown in Figure 8a for two values of total blast impulse I_0. Deformation of the square honeycomb core is concentrated at the impacted face sheet [21]. The corrugated core specimens debonded at the glued interface between the core assembly and the back face sheet. This spalling of the back face occurred in most specimens of the corrugated core (and for none of the square honeycomb specimens).

The horizontal lines of constant I_t / I_0 in Figures 7b and 7c represent the Taylor [20] free-standing rigid plate predictions for (i) a plate with mass equal to the sandwich plates (labelled $\psi = \psi_t$) , and (ii) a plate with mass equal to the front face sheet (labelled $\psi = \psi_f$). Results for both core types lie within these rigid plate limits. Sandwich construction (with either topology) therefore offers a benefit over monolithic construction in terms of imparted momentum. The free-standing rigid face sheet limit is not reached, indicating that core deformation and fluid-structure interaction are coupled. These observations are qualitatively consistent with the conclusions from a number of numerical studies [3-6].

The normalised imparted momentum to the sandwich specimens with a square honeycomb core is largely insensitive to the intensity of the applied loading for each series. In contrast, for the corrugated core, I_t / I_0 increases with increasing I_0 prior to the onset of core densification. At comparable values of I_0 the normalised imparted momentum I_t / I_0 is similar for the two core topologies.

4.2 Sensitivity of the response to ψ_f

Recall that ψ_f for series 2 is double that for series 1 (achieved by redistributing the mass ratio m_f / m_b from 1 to 1/3 for series 1 and 2, respectively). ψ_t is held constant as both m_t and θ are fixed for the two series of tests. A comparison of the results for series 1 and 2 reveals the following effects.

(i) For a given total blast impulse I_0, the normalised imparted momentum I_t / I_0 is slightly lower for series 2 than for series 1. This can be explained by the earlier onset of cavitation in the fluid with a reduction in the mass of the impacted face sheet.

(ii) Both core topologies show larger core compressions for series 2 than for series 1. Although the total momentum imparted to the sandwiches is reduced, the kinetic energy is higher for the lighter front face. This results in greater core compression. For a structural panel, this increased core compression is detrimental to the residual bending stiffness and strength.

4.3 Sensitivity of the response to ψ_t

The sensitivity of I_t / I_0 to ψ_t is shown in Figure 7c for both cores, with ψ_f held fixed. Doubling ψ_t significantly reduces I_t / I_0: compare series 2 and 3 for each core in turn. Recall from Figure 7b that the sensitivity of I_t / I_0 to ψ_f is more modest. Doubing ψ_t also results in a lower core compression, and a total imparted impulse which is closer to the result for a monolithic plate of mass m_t.

5. Finite element analysis

In order to gain further insight into the fluid-structure interaction, three-dimensional finite element calculations have been performed using the commercially available code ABAQUS/Explicit. Details of the modelling procedure, including the component geometries, material properties, finite element meshes and initial geometric imperfections are given in Appendix B. All parameters are chosen to replicate the experimental conditions.

5.1 Quasi-static compression of the cores

First, we compare experimental measurements and finite element calculations of the quasi-static compressive response of the two core topologies. For these calculations, only the core models described in Appendix B are included, with the face sheets modelled as rigid surfaces. The explicit time integration version of ABAQUS (as used for the dynamic calculations) is employed for the quasi-static simulations. Constraints on the face sheet motion match those of the quasi-static experiments. The results are plotted in Figure 3 and show good agreement with the experimental measurements, except for the peak stress which is imperfection-sensitive.

5.2 Characteristic transient response of the structure

Finite element calculations were performed to model the experiments detailed in Table 1. The predicted time evolution of the transmitted impulse from the water I, the stress σ_f between the front face and the core, and the nominal core strain ε_N are plotted in Figure 9 for the square honeycomb and corrugated core sandwich plates. Results are shown only for an impulse $I_0 = 30$ kPas of series 1. The deformation history for each core type comprises a sequence of three phases and is now summarised; the qualitative details are the same for all simulations conducted on a given core. First consider the response of the corrugated core and then that of the square honeycomb.

The corrugated core plate. In phase I, the front face is accelerated by the water, with negligible resistance from the core and rear face. The front face acquires the Taylor value of impulse (given by Eq. (5) with $\psi = \psi_f$) over a timescale on the order of 0.5θ, and cavitation ensues. At the onset of cavitation, the front face has acquired a high velocity while the core and back face are almost stationary. Phase II ensues for $0.5 < t/\theta < 1.8$, see Figure 9. The front face is in free-flight, as the water is cavitated and the corrugated core continues to have negligible strength, see Figure 9b. At $t/\theta \approx 1.8$ the core densifies and the front face slaps into the back face. During the densification event $1.8 < t/\theta < 2.0$ the core strength σ_f displays a transient high value (Figure 9b) and the front face is abruptly retarded to about half its velocity. The cavitated water adjacent to the front face reconstitutes and loads the front face: the transmitted impulse I increases from $0.16\,I_0$ to $0.20\,I_0$ (Figure 9a). At $t/\theta \approx 2.0$, the front and back faces have acquired a common velocity, the core stress drops to almost zero and water adjacent to the front face re-cavitates. Thereafter, the sandwich panel undergoes free-flight, and we term this phase III.

The square honeycomb core plate. In phase I the front face accelerates and cavitation ensues at $t/\theta \approx 0.5$. The momentum imparted in phase I is close to the Taylor value for a free-standing front face sheet, and is similar to the corrugated core sandwich. In phase II, the core has significant strength and the front face is retarded. The cavitated water adjacent to the front face reconstitutes and loads the front face throughout phase II. Consequently I/I_0 rises slightly (Figure 9a). At the end of phase II, $t/\theta \approx 2.5$, the front and back faces equalise in velocity before the core has fully densified. Thereafter, the sandwich plate behaves as a monolithic plate of mass m_t. A second cavitation event occurs at $t/\theta \approx 2.6$ and thereafter the sandwich plate travels in free-flight (phase III). The total imparted momentum is similar to the corrugated core sandwich.

5.3 Dynamic fluid-structure interaction calculations

Calculations were performed for selected values of blast peak pressure p_0, spanning a range of total blast impulse I_0 similar to the experimental measurements. The predicted response for $\left(I_t/I_0,\ \varepsilon_C\right)$ versus I_0 is in good agreement with measured values for the square honeycomb core, see Figure 10. In contrast, the agreement for the corrugated core is poor, see Figure 11. The precise reason for this is unclear but it is most likely related to the debonding of the distal face sheet during the FSI event, recall the examples shown in Figure 8a. This debonding effect was not included in the FE model (calculated deformed shapes are shown in Figure 8b for comparison with the experimental specimens). To accurately capture this effect, the dynamic cohesive properties of the adhesive layer would need to be evaluated and incorporated into the model. A study of the role of interface behaviour is beyond the scope of the present investigation, but these experiments highlight the need for strong bonds at the local attachment points between lattice core and face-sheet.

6. Concluding remarks

A water tube apparatus has been used to measure the FSI effects during underwater blast loading of free-standing sandwich plates with metallic lattice cores. The FSI parameters were systematically varied. For both types of sandwich core considered in this study (the square honeycomb and the corrugated core) two cavitation events occur:

(i) An initial cavitation event is associated with the early acceleration of the front face, with the transmitted impulse dictated by ψ_f.

(ii) A second cavitation event occurs after the sandwich core has compressed, when the sandwich is behaving as a monolithic plate.

The total transmitted impulse scales primarily with ψ_t rather than ψ_f for both cores. This is due to the fact that the initial FSI event associated with the front face is followed by a second FSI (and cavitation) event where the water interacts with the entire sandwich plate. Consequently the final transmitted impulse for the sandwich plate may be better approximated by the Taylor analysis for a free-standing monolithic plate of mass equal to that of the sandwich, rather than the Taylor analysis for a free standing front face sheet. The main effect of core topology is to dictate the final degree of core compression: the stronger the core, the smaller the core compression. A reduced core compression has the advantage of maintaining a sandwich effect after blast loading.

The sensitivity of the total transmitted impulse I_t / I_0 to the loading parameters and to the geometry are adequately predicted by finite element simulations. An acoustic approximation is able to capture the cavitation response for practical levels of shock pressures on the order of 100 MPa.

Acknowledgements

The authors are grateful for financial support from the Office of Naval Research (N00014-07-1-0114) and from the EPSRC (EP/D055806/1).

Appendix A: Manufacture of the sandwich specimens

Each sandwich specimen consists of a front face sheet, a core assembly and a back face-sheet, as illustrated in Figure A1. The cores have a diameter of $58\ \mathrm{mm}$, which is slightly less than the face sheet diameter of $D = 64\ \mathrm{mm}$. This clearance is included to allow for some lateral expansion of the core during crushing within the water blast apparatus. The fabrication route for each lattice core assembly is as follows:

Square-honeycomb core. Following the technique of Côté et al. [23], rectangular slotted combs of AISI 304 stainless steel sheet (thickness $a = 0.3\ \mathrm{mm}$) are assembled as shown in Figure A1b to form the square honeycomb. Circular discs of diameter $58\ \mathrm{mm}$ are cut from the same stainless steel sheet and are used as intermediate face sheets (Figure A1b). These intermediate face sheets are included to provide a strong bond between the core and the aluminium face sheets, as follows. The core and intermediate face sheets are first joined by brazing for one hour at $1065°\mathrm{C}$ using a uniform coating of nickel-based brazing alloy. This produces strong joints between the core plates and between the core and the stainless steel intermediate face sheets. The intermediate face sheets provide a large surface area to permit bonding of the core assembly to the aluminium main face sheets using a room-temperature curing structural epoxy adhesive.

Corrugated core. A corrugated core sandwich beam is first assembled from stainless steel sheet of thickness $a = 0.3\ \mathrm{mm}$, see Figure A1c. The corrugations are spot-welded to rectangular front and back intermediate face sheets. The back intermediate face sheet is turned up at the edges to an angle of $60°$ to support the outermost legs of the corrugation and strengthen the joint, as shown in the Figure. The assembly is then brazed, as described for the square honeycomb. Individual cylindrical core assemblies of diameter $58\ \mathrm{mm}$ are cut from the brazed beams using a high pressure water jet as indicated in Figure A1c. Finally, the core assembly is bonded to the aluminium face sheets using an epoxy adhesive.

Appendix B: Finite element modelling procedure

Three-dimensional finite element calculations were performed using the commercially available code ABAQUS/Explicit. In all calculations, the ABAQUS automatic time incrementation was used, which is based on a continuously updating estimate of the stable time step. A representative finite element model for the water column and square honeycomb core sandwich specimen from test series 1 is shown in Figure B1. Each component of the finite element model will now be described.

Fluid column: The fluid is modelled in ABAQUS as an acoustic medium of density $\rho_w = 1000$ kgm^{-3}, bulk modulus $K_w = 1.96$ GPa and wave speed $c_w = \sqrt{K_w / \rho_w} = 1400$ ms^{-1}. It is assumed that the water cannot support tension, such that the cavitation pressure is $p_{cav} = 0$. The column is circular in cross-section with diameter $D = 64$ mm. It is discretized using a mixture of 8-noded hexahedral acoustic brick elements with reduced integration and 6-noded acoustic triangular wedge elements (AC3D8R and AC3D6, respectively, in ABAQUS notation). There are approximately 15 elements radially, matched to the mesh size of the sandwich front face sheet (which is tied to one end of the water column) such that the nodes of the acoustic and solid meshes coincide. An element size of 4 mm is used along the length-direction z of the column. The top end of the water column is loaded by a transient pressure pulse in accordance with equation (1). In order to validate the mesh used to represent the fluid column, the momentum imparted to a circular rigid plate with mass per unit area 99 kgm^{-2} was calculated for I_0 = 10, 20 and 30 kPas with $\theta = 0.13$ ms. The calculated results agreed with the Taylor [20] solution $I_t / I_m = 1$ to within 0.02%.

Sandwich face sheets: The front and back face sheets are modelled as circular plates of diameter $D = 64$ mm and thicknesses H_f and H_b respectively. In order to simplify the geometry, the stainless steel intermediate face sheets are not modelled separately. The thicknesses H_f and H_b are chosen so that the face sheet masses in the finite element calculations match the mass of the aluminium face sheet plus the stainless-steel intermediate face sheet used in each experiment. The sides of the face sheets are in sliding contact with the inner surface of the steel tube (Figure 4), and are constrained as shown in Figure B1. The face sheets are discretized using a combination of 8-noded hexahedral brick elements with reduced integration and 6-noded triangular wedge elements (C3D8R and C3D6, respectively, in ABAQUS notation). There are approximately 15 elements radially, and an element size of 2 mm is used though the plate thickness. The material model used for the face sheets in the calculations is representative of 6082-T6 aluminium alloy, with density $\rho = 2710\ \text{kgm}^{-3}$, Young's modulus $E = 70\ \text{GPa}$ and Poisson's ratio $\nu = 0.3$. An elastic, ideally plastic response is assumed, with yield stress $\sigma_Y = 285\ \text{MPa}$. However, the face sheets undergo negligible plastic deformation in both the experiments and the finite element calculations.

Sandwich cores: The dimensions of the circular metallic lattice cores in the finite element model are chosen to match exactly the experimental specimens as given in Figures 1a and 1b for the corrugated and square honeycomb cores respectively. The stainless-steel plates of the cores are discretized using linear quadrilateral shell elements with reduced integration (S4R in ABAQUS terminology). The shell elements are approximately square with side length $0.5\ \text{mm}$, and the shell thickness $a = 0.3\ \text{mm}$, equal to the stainless steel plate thickness prior to brazing. Any additional mass and plate thickness introduced by brazing is neglected. Consequently the total sandwich masses in the numerical models are slightly less than the experimental specimens: $m_t = 97\ \text{kgm}^{-2}$ for the corrugated core sandwich and $m_t = 99\ \text{kgm}^{-2}$ for the square honeycomb in the finite element calculation, compared to $98\ \text{kgm}^{-2}$ and $100\ \text{kgm}^{-2}$ for the experimental specimens. Hard, frictionless contacts are defined between all surfaces in the model to allow densification of the core. A tie constraint is applied between the edges of the core and the face sheets where they are in contact, indicated by the dashed lines in Figure B1. Additionally, all rotational degrees of freedom are set to zero for the tied shell element nodes, representative of an ideally brazed joint.

The AISI 304 stainless steel used for the core is modelled as a J_2 flow theory rate-dependent solid. The density $\rho = 7950\ \text{kgm}^{-3}$, Young's modulus $E = 210\ \text{GPa}$ and Poisson's ratio $\nu = 0.3$. The true stress versus logarithmic plastic strain curves used in these calculations to represent brazed AISI 304 stainless steel are plotted in Figure 2. The high strain rate response is related to the measured quasi-static curve through a strain-rate dependent multiplier R, which is assumed to be independent of plastic strain. The values of R used here are taken from the results of Stout and Follansbee [26].

An initial geometric imperfection is introduced into each core topology by perturbing the finite element mesh using one or more static elastic buckling mode shapes superimposed. The sensitivity of each core topology to the initial imperfection was systematically investigated as follows. Water blast calculations were performed with the parameters $m_f = m_b = 47\ \text{kgm}^{-2}$, $\theta = 0.13\ \text{ms}$, $p_0 = 19.4\ \text{MPa}$ for the corrugated core and $p_0 = 77.5$ MPa for the square honeycomb. These peak pressures were chosen to give a maximum core compression of around $\varepsilon_c = 0.30$ for each topology. For each core, a series of calculations were performed with an increasing number of superimposed mode shapes in the initial mesh perturbation. This process was repeated for a range of peak imperfection amplitudes, δ. Note that each mode shape was initially normalised such that that maximum component of displacement is equal to 1. They were then superimposed and scaled, with an equal scale factor applied to each mode, to give the required imperfection amplitude. The sensitivity to both the amplitude and number of modes was determined by examining the effect on the maximum core compression and the total transmitted momentum. For both cores, the total imparted momentum was insensitive to the choice of imperfection (varying by no more than 3% over a wide range of imperfection types and amplitudes, but generally decreasing with increasing imperfection amplitude), so the maximum core compression was considered the critical criterion.

For the square honeycomb core, increasing both the imperfection amplitude and the number of superimposed mode shapes resulted in an increase in maximum core compression. The chosen imperfection was such that further increases in the number of modes or the peak amplitude made no significant difference to the calculated core compression: the first 200 modes superimposed was used with a total peak amplitude $\delta / a = 1$, where $a = 0.3$ mm is the thickness of the stainless steel plates in the core. For the corrugated core, it was observed that introducing the first buckling mode only increased the maximum core compression compared to the zero imperfection result. However, introducing a superposition of multiple modes reduced the maximum core compression compared to the mode 1 perturbation (for a fixed total imperfection amplitude). It was therefore inferred that the critical mode for this core is mode 1, and the chosen imperfection was the first mode alone with a peak amplitude $\delta / a = 1$.

References

1. Fleck NA, Deshpande VS. The resistance of clamped sandwich beams to shock loading. Journal of Applied Mechanics 2004; 71: 386-401.

2. Xue Z, Hutchinson JW. A comparative study of blast-resistant metal sandwich plates. International Journal of Impact Engineering 2004; 30: 1283-1305.

3. Deshpande VS, Fleck NA. One-dimensional response of sandwich plates to underwater shock loading. Journal of the Mechanics and Physics of Solids 2005; 53: 2347-2383.

4. Rabczuk T, Samaniego E, Belytschko T. Simplified model for predicting the impulsive loads on submerged structures to account for fluid-structure interaction. International Journal of Impact Engineering 2007; 34: 163-177.

5. Liang Y, Spuskanyuk AV, Flores SE, Hayhurst DR, Hutchinson JW, McMeeking RM, Evans AG. The response of metallic sandwich panels to water blast. Journal of Applied Mechanics 2007; 74: 81-99.

6. McShane GJ, Deshpande VS, Fleck NA. The underwater blast resistance of metallic sandwich beams with prismatic lattice cores. Journal of Applied Mechanics 2007; 74: 352-364.

7. Tilbrook MT, Deshpande VS, Fleck NA. The impulsive response of sandwich beams: Analytical and numerical investigation of regimes of behaviour. Journal of the Mechanics and Physics of Solids 2006; 54: 2242-2280.

8. Chiras S, Mumm DR, Evans AG, Wicks N, Hutchinson JW, Dharmasena K, Wadley HNG, Fichter S. The structural performance of near-optimized truss core panels. International Journal of Solids and Structures 2002; 39: 4093-4115.

9. Valdevit L, Hutchinson JW, Evans AG. Structurally optimized sandwich panels with prismatic cores. International Journal of Solids and Structures 2004; 41: 5105-5124.

10. Radford DD, Fleck NA, Deshpande VS. The response of clamped sandwich beams subjected to shock loading. International Journal of Impact Engineering 2006; 32: 968-987.

11. Rathbun HJ, Radford DD, Xue Z, He MY, Yang J, Deshpande V, Fleck NA, Hutchinson JW, Zok FW, Evans AG. Performance of metallic honeycomb-core sandwich beams under shock loading. International Journal of Solids and Structures 2006; 43: 1746-1763.

12. Wei Z, Dharmasena KP, Wadley HNG, Evans AG. Analysis and interpretation of a test for characterizing the response of sandwich panels to water blast. International Journal of Impact Engineering 2007; 34: 1602-1618.

13. Wadley H, Dharmasena K, Chen Y, Dudt P, Knight D, Charette R, Kiddy K. Compressive response of multilayered pyramidal lattices during underwater shock loading. International Journal of Impact Engineering 2008; 35: 1102-1114.

14. Deshpande VS, Heaver A, Fleck NA. An underwater shock simulator. Proceedings of the Royal Society A 2006; 462: 1021-1041.

15. Cole RH. Underwater Explosions. Princeton University Press, Princeton, 1948.

16. Swisdak MM. Explosion effects and properties – Part II: Explosion effects in water. Technical Report, Naval Surface Weapons Centre, Dahlgren, VA, USA, 1978.

17. Espinosa HD, Lee S, Moldovan N. A novel fluid-structure interaction experiment to investigate deformation of structural elements subjected to impulsive loading. Experimental Mechanics 2006; 46: 805-824.

18. Mori LF, Lee S, Xue ZY, Vaziri A, Queheillalt DT, Dharmasena KP, Wadley HNG, Hutchinson JW, Espinosa HD. Deformation and fracture modes of sandwich structures subjected to underwater impulsive loads. Journal of Mechanics of Materials and Structures 2007; 2: 1981-2006.

19. Mori LF, Queheillalt DT, Wadley HNG, Espinosa HD. Deformation and failure modes of I-core sandwich structures subjected to underwater impulsive loads. Experimental Mechanics 2009; 49: 257-275.

20. Taylor GI. The pressure and impulse of submarine explosion waves on plates. In: The Scientific Papers of G.I. Taylor, Volume III, pp. 287-303. Cambridge University Press, Cambridge, 1963.

21. Radford DD, McShane GJ, Deshpande VS, Fleck NA. Dynamic compressive response of stainless-steel square honeycombs. Journal of Applied Mechanics 2007; 74: 658-667.

22. Tilbrook MT, Radford DD, Deshpande VS, Fleck NA. Dynamic crushing of sandwich panels with prismatic lattice cores. International Journal of Solids and Structures 2007; 44: 6101-6123.

23. Côté F, Deshpande VS, Fleck NA, Evans AG. The out-of-plane compressive behaviour of metallic honeycombs. Materials Science and Engineering A 2004; 380: 272-280.

24. Vaughn DG, Canning JM, Hutchinson JW. Coupled plastic wave propagation and column buckling. Journal of Applied Mechanics 2005; 72: 139-146.

25. St-Pierre L, Deshpande VS, Fleck NA. The three-point bending response of sandwich beams with corrugated and Y-frame cores: does the back face contribute to the structural performance? Manuscript in preparation.

26. Stout MG, Follansbee PS. Strain-rate sensitivity, strain hardening and yields behaviour of 304L stainless steel. Journal of Engineering Materials Technology 1986; 108: 344-353.

27. Calladine CR, English RW. Strain-rate and inertia effects in the collapse of two types of energy absorbing structures. International Journal of Mechanical Sciences 1984; 26: 689-701.

Figure Captions

Table 1: Experimental parameters. For each series, averages of the measured values are given separately for the square honeycomb core and corrugated core sandwiches. Quoted face sheet masses include the intermediate face sheets, the adhesive layer and (for the front face) the O-ring. Core masses are measured after brazing.

Figure 1: Metallic lattice core sandwich plate geometries: (a) corrugated core sandwich, (b) square honeycomb core sandwich. The detail in (b) shows the dimensions of the square honeycomb. The face sheet thicknesses are chosen to fix their masses as required by each test series.

Figure 2: The measured quasi-static tensile response of the 0.3 mm thickness brazed AISI 304 stainless steel sheet ($\dot{\varepsilon}$ = 10^{-3} s^{-1}). The tensile response at higher strain rates is inferred from the data of Stout and Follansbee [26].

Figure 3: Quasi-static nominal stress (σ_N) versus nominal compressive strain (ε_N) response of (a) the square honeycomb core and (b) the corrugated core. Experimental measurements (solid lines) and finite element calculations (dashed lines) are shown.

Figure 4: The apparatus used in the dynamic experiments, adapted from the method of Deshpande et al. [14].

Figure 5: High speed photographic sequence ($247\,\mu\text{s}$ inter-frame time) showing a square honeycomb core sandwich specimen emerging from the laser velocity gauge at the exit of the water blast apparatus. The blast pulse peak pressure $p_0 = 85$ MPa and the decay constant $\theta = 0.26$ ms.

Figure 6: Experimental technique for measuring the maximum core compression of the corrugated core sandwiches during the dynamic tests. (a) A folded strip of metallic foam is placed inside the central corrugation, held in place by friction only. (b) The foam insert is crushed with the core, but (c) retains its crushed shape if the faces separate.

Figure 7: Experimental measurements of (a) the maximum core compression, (b) the transmitted momentum (series 1 and 2) and (c) the transmitted momentum (series 2 and 3). Taylor [20] estimates of the momentum imparted to rigid plates of mass equal to the total sandwich ($\psi = \psi_t$) and the front face sheet alone ($\psi = \psi_f$) are marked in (b) and (c).

Figure 8: (a) Experimental results and (b) finite element calculations of the deformed core shapes for square honeycomb core and corrugated core sandwiches from series 1. The front face (wet face) is shown uppermost, indicated by the O-ring in the experimental specimens.

Figure 9: Finite element calculations of the time dependent (a) momentum imparted by the blast (the Taylor [20] rigid plate solutions are indicated), (b) stress exerted by the core on the front face sheet and (c) nominal core compression, for the square-honeycomb core and corrugated core sandwiches (series 1, I_0 = 30 kPas). In (b) $\sigma_y = 297$ MPa is the initial yield strength of the stainless steel.

Figure 10: Experimental results and finite element (FE) calculations for the square honeycomb core sandwich plates showing (a) core compression, (b) transmitted momentum (series 1 and 2) and (c) transmitted momentum (series 2 and 3). Taylor [20] estimates of the momentum imparted to rigid plates of mass equal to the total sandwich ($\psi = \psi_t$) and the front face sheet alone ($\psi = \psi_f$) are marked in (b) and (c).

Figure 11: Experimental results and finite element (FE) calculations for the corrugated core sandwich plates showing (a) core compression, (b) transmitted momentum (series 1 and 2) and (c) transmitted momentum (series 2 and 3). Taylor [20] estimates of the momentum imparted to rigid plates of mass equal to the total sandwich ($\psi = \psi_t$) and the front face sheet alone ($\psi = \psi_f$) are marked in (b) and (c).

Figure A1: Fabrication method for the experimental sandwich specimens: (a) sandwich assembly, (b) square honeycomb core and (c) corrugated core.

Figure B1: Boundary conditions used in the finite element analysis of the sandwich plate fluid-structure interaction.

	front face m_f $\left(\mathrm{kg}\times10^{-3}\right)$	back face m_b $\left(\mathrm{kg}\times10^{-3}\right)$	core m_c $\left(\mathrm{kg}\times10^{-3}\right)$	sandwich m_t $\left(\mathrm{kg}\times10^{-3}\right)$	θ (ms)	ψ_f	ψ_t
Series 1							
honeycomb	151	151	20.7	322	0.132	3.93	1.84
corrugated	152	150	13.8	316	0.127	3.76	1.81
Series 2							
honeycomb	76.6	224	20.9	321	0.125	7.36	1.75
corrugated	76.8	222	13.9	313	0.117	6.85	1.68
Series 3							
honeycomb	151	152	20.8	323	0.267	7.99	3.72
corrugated	151	149	13.9	314	0.240	7.17	3.45

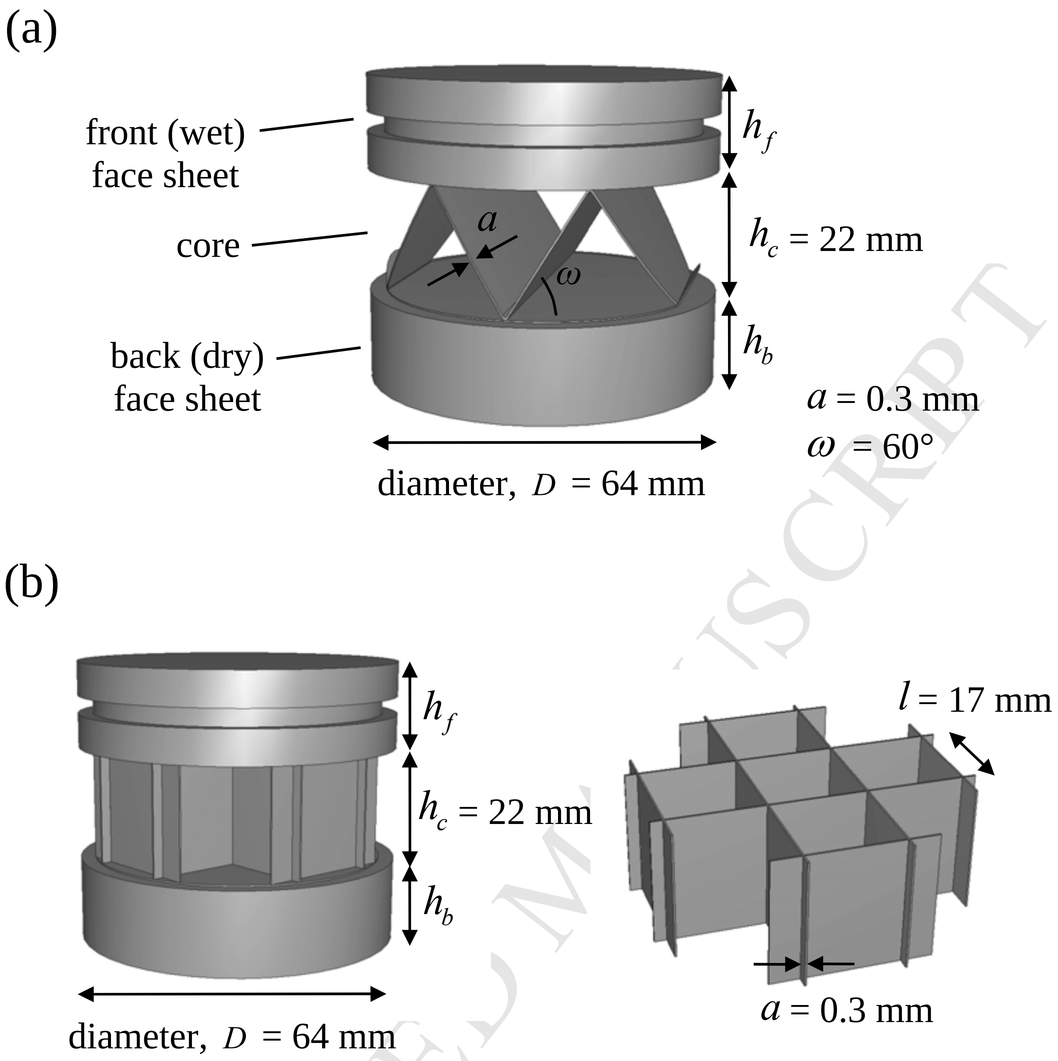
(a)
front (wet)
face sheet
core
back (dry)
face sheet
a
ω
h_f
h_c = 22 mm
h_b
a = 0.3 mm
ω = 60°
diameter, D = 64 mm
(b)
h_f
h_c = 22 mm
h_b
diameter, D = 64 mm
l = 17 mm
a = 0.3 mm

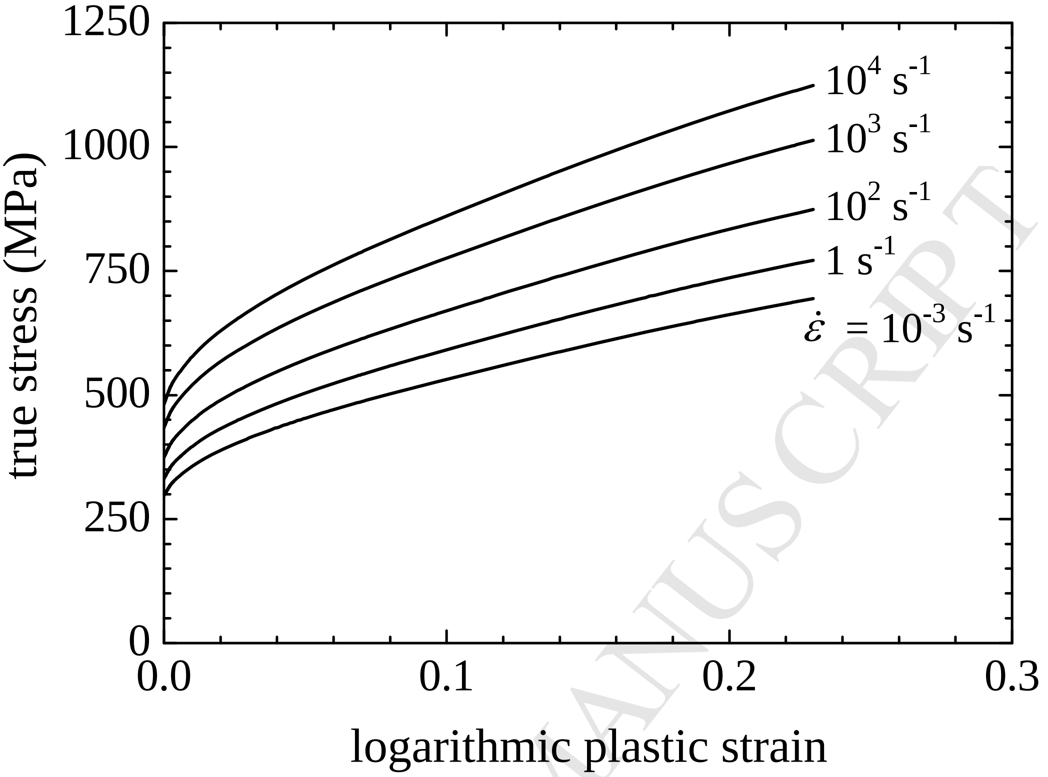
1250
1000
750
500
250
0
true stress (MPa)
0.0
0.1
0.2
0.3
logarithmic plastic strain
10^4 s^{-1}
10^3 s^{-1}
10^2 s^{-1}
1 s^{-1}
$\dot{\varepsilon}$ = 10^{-3} s^{-1}

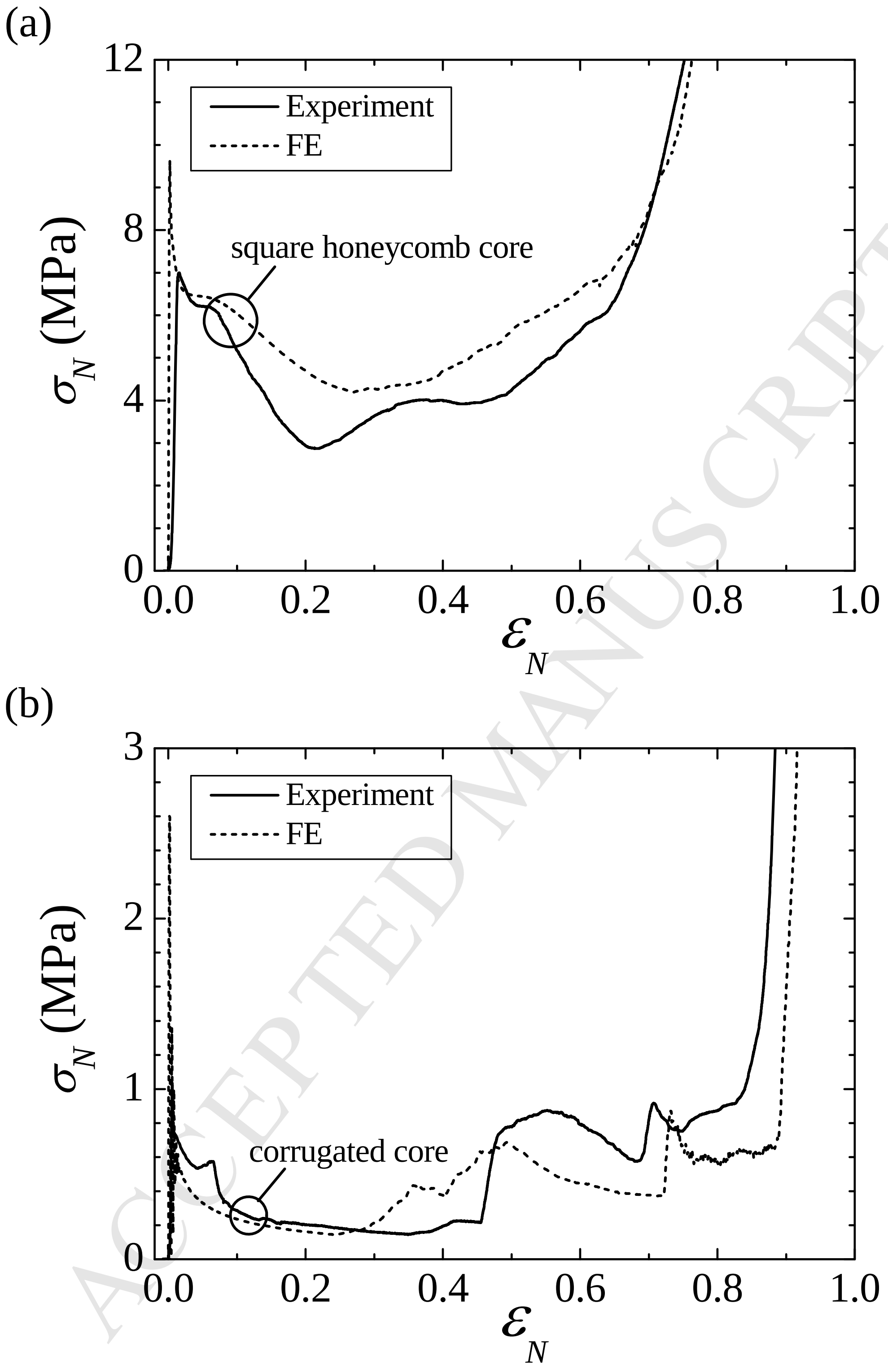
(a)
12
8
4
0
σ_N (MPa)
0.0
0.2
0.4
0.6
0.8
1.0
ε_N
Experiment
FE
square honeycomb core
(b)
3
2
1
0
σ_N (MPa)
0.0
0.2
0.4
0.6
0.8
1.0
ε_N
Experiment
FE
corrugated core

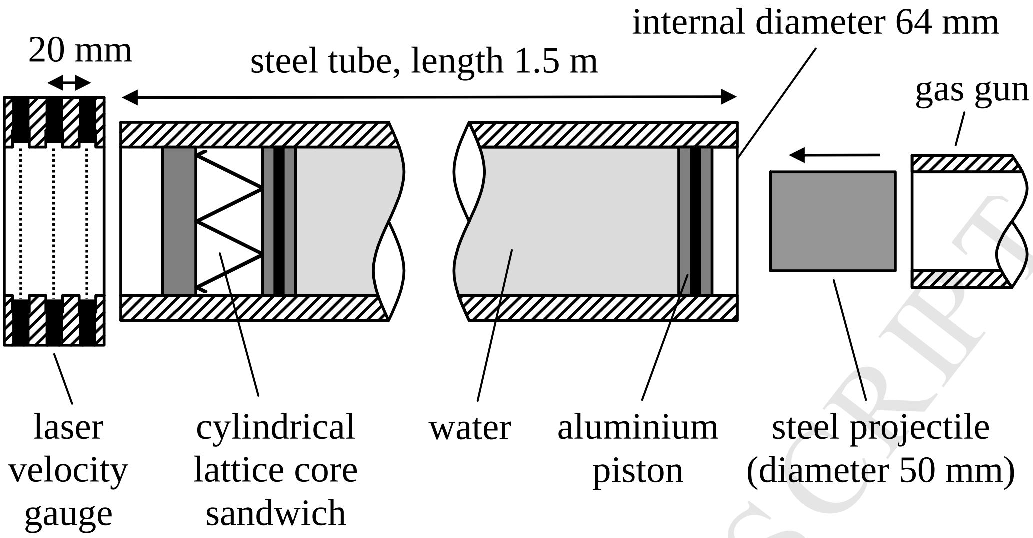
internal diameter 64 mm
20 mm
steel tube, length 1.5 m
gas gun
laser velocity gauge
cylindrical lattice core sandwich
water
aluminium piston
steel projectile (diameter 50 mm)

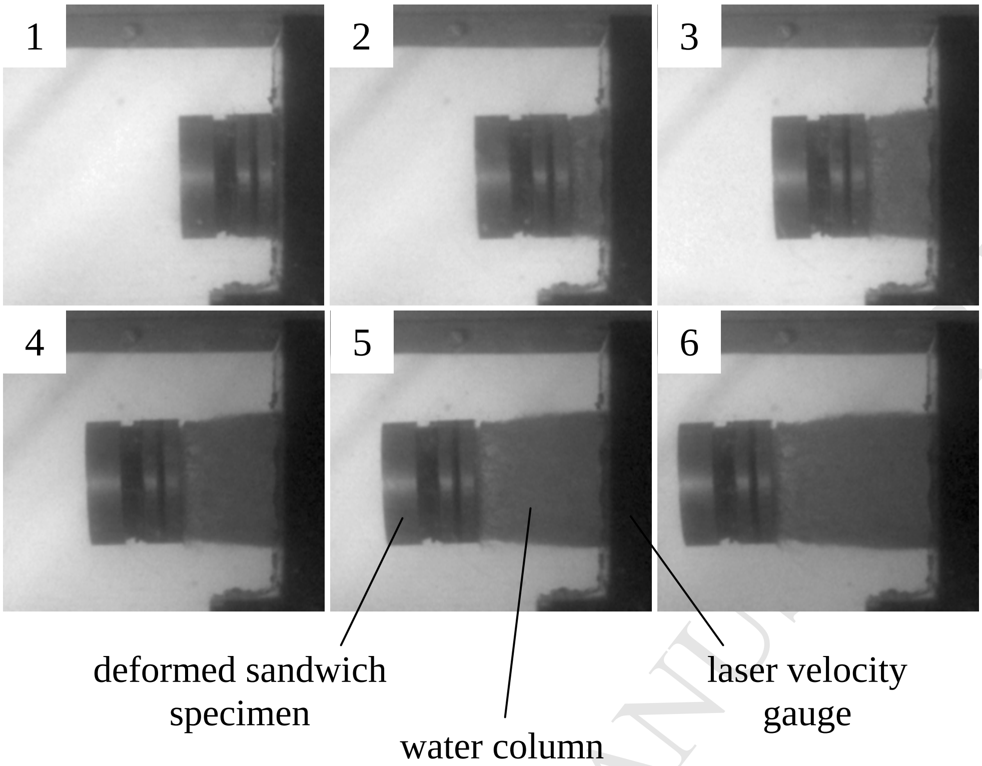
1
2
3
4
5
6
deformed sandwich specimen
water column
laser velocity gauge

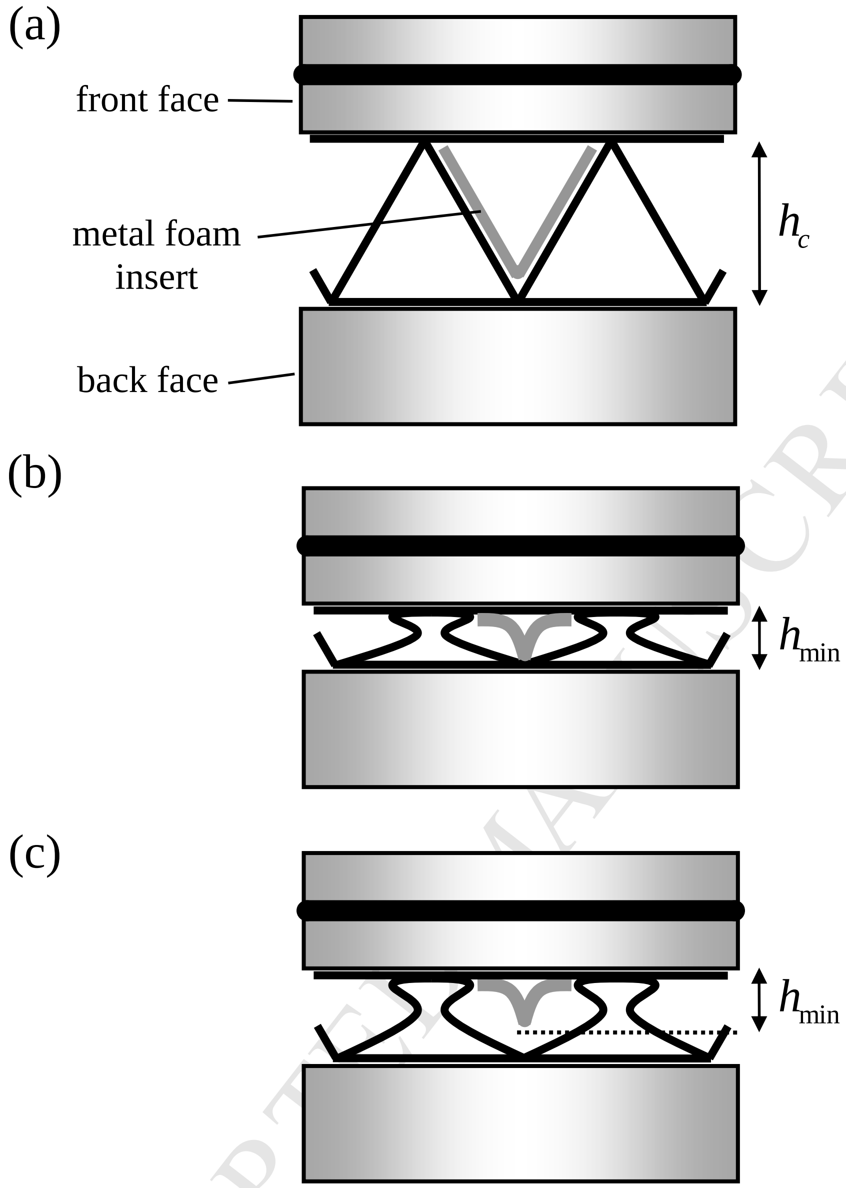
(a)
front face
metal foam insert
back face
h_c
(b)
h_{min}
(c)
h_{min}

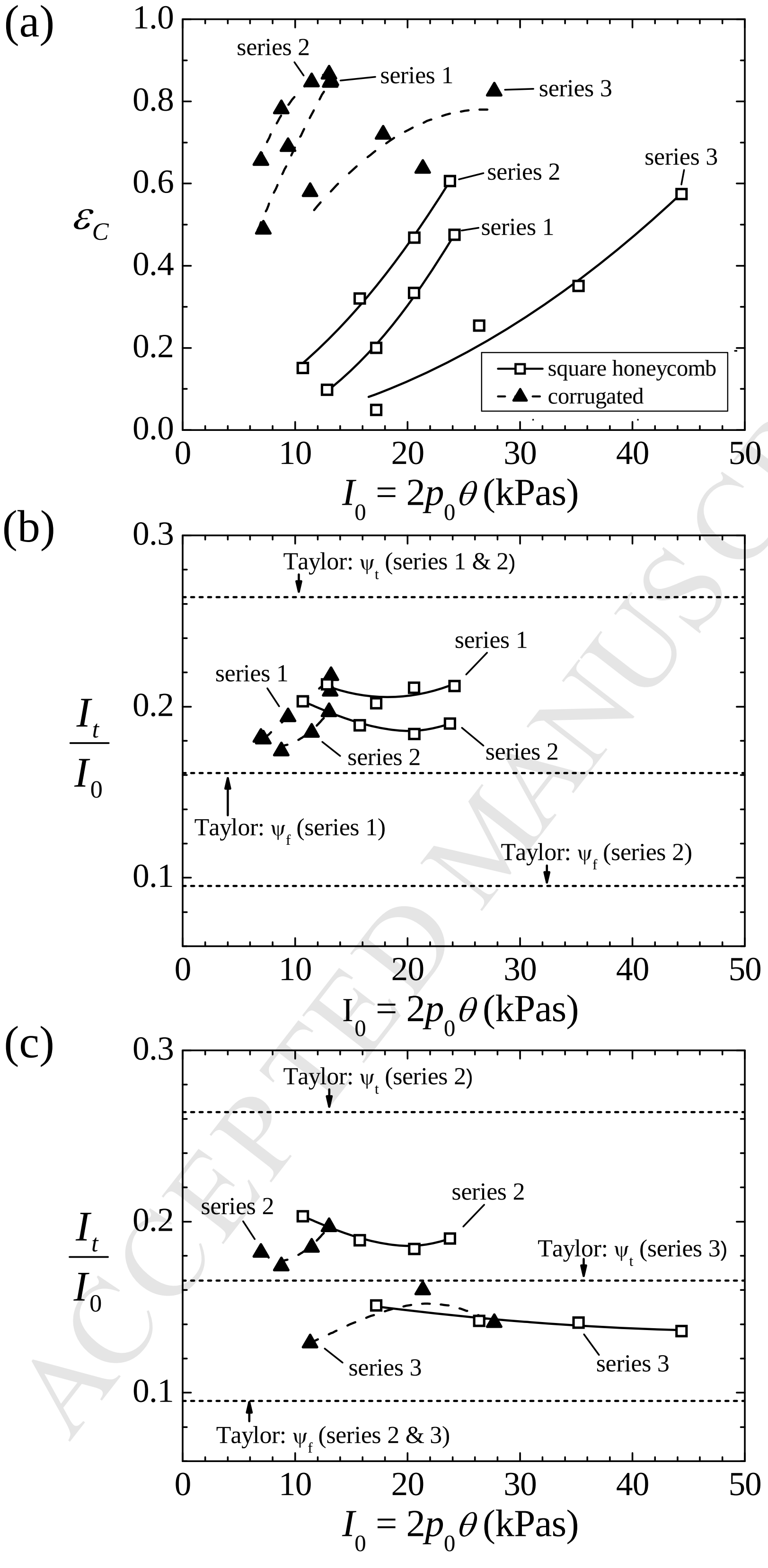
(a)
1.0
0.8
0.6
0.4
0.2
0.0
ε_C
series 2
series 1
series 3
series 2
series 3
series 1
square honeycomb
corrugated
0
10
20
30
40
50
$I_0 = 2p_0\theta$ (kPas)
(b)
0.3
0.2
0.1
Taylor: ψ_t (series 1 & 2)
series 1
series 1
series 2
series 2
Taylor: ψ_f (series 1)
Taylor: ψ_f (series 2)
$\frac{I_t}{I_0}$
0
10
20
30
40
50
$I_0 = 2p_0\theta$ (kPas)
(c)
0.3
0.2
0.1
Taylor: ψ_t (series 2)
series 2
series 2
Taylor: ψ_t (series 3)
series 3
series 3
Taylor: ψ_f (series 2 & 3)
$\frac{I_t}{I_0}$
0
10
20
30
40
50
$I_0 = 2p_0\theta$ (kPas)

(a)

Square Honeycomb $\theta = 0.13$ ms $m_f / m_b = 1$	 $I_0 = 13$ kPas	 $I_0 = 21$ kPas
Corrugated $\theta = 0.13$ ms $m_f / m_b = 1$	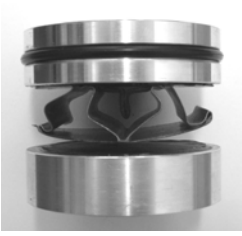 $I_0 = 7$ kPas	 $I_0 = 13$ kPas

(b)

Square Honeycomb $\theta = 0.13$ ms $m_f / m_b = 1$	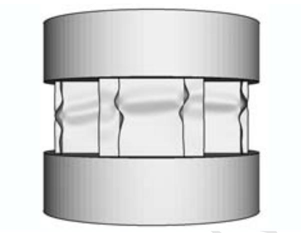 $I_0 = 10$ kPas	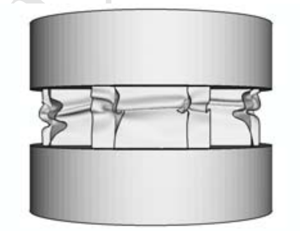 $I_0 = 20$ kPas
Corrugated $\theta = 0.13$ ms $m_f / m_b = 1$	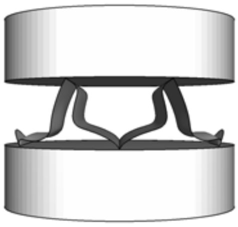 $I_0 = 5$ kPas	 $I_0 = 15$ kPas

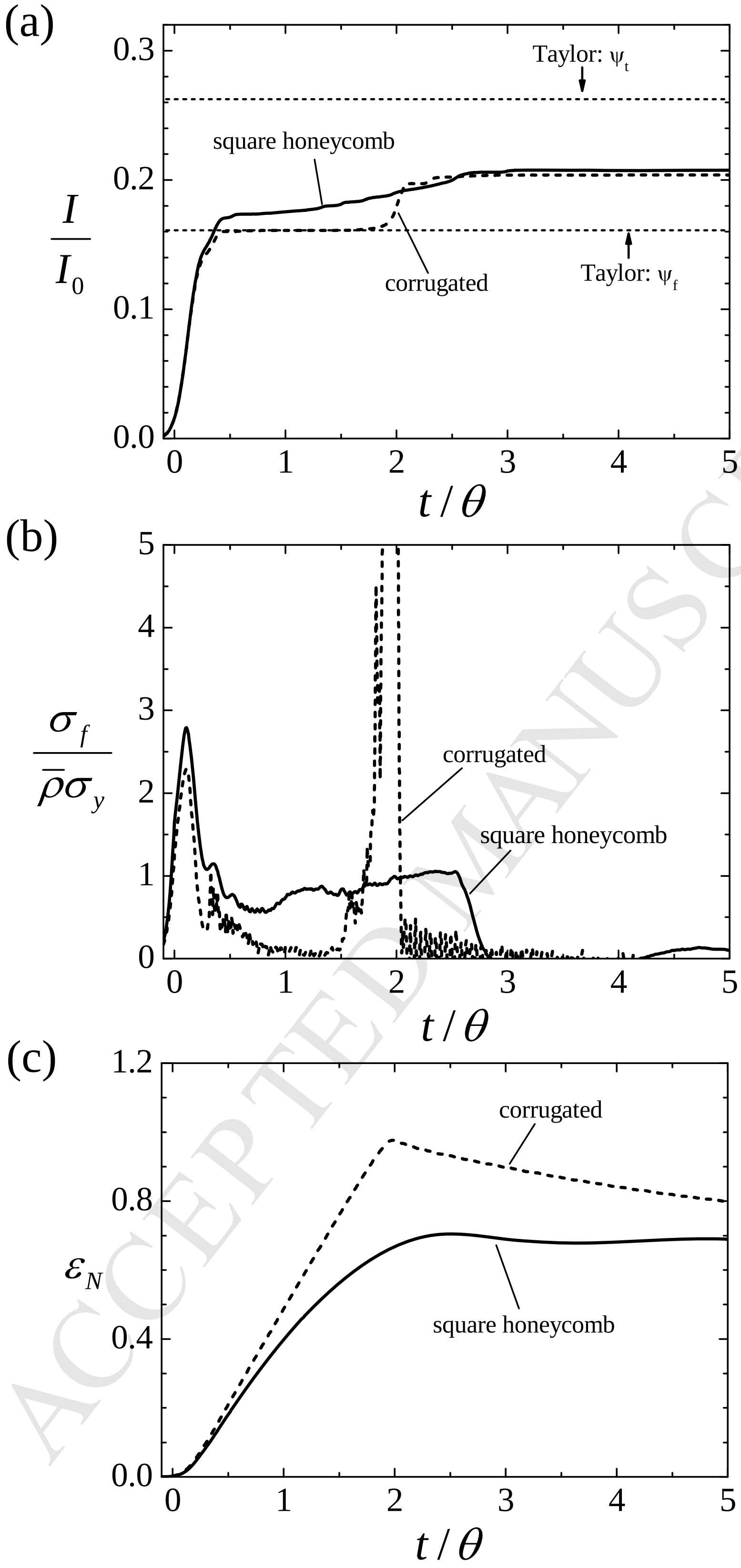
(a)
0.3
0.2
0.1
0.0
Taylor: ψ_t
square honeycomb
I / I_0
corrugated
Taylor: ψ_f
0
1
2
3
4
5
t / θ
(b)
5
4
3
2
1
0
σ_f / ρ̄σ_y
corrugated
square honeycomb
t / θ
(c)
1.2
0.8
0.4
0.0
ε_N
corrugated
square honeycomb
t / θ

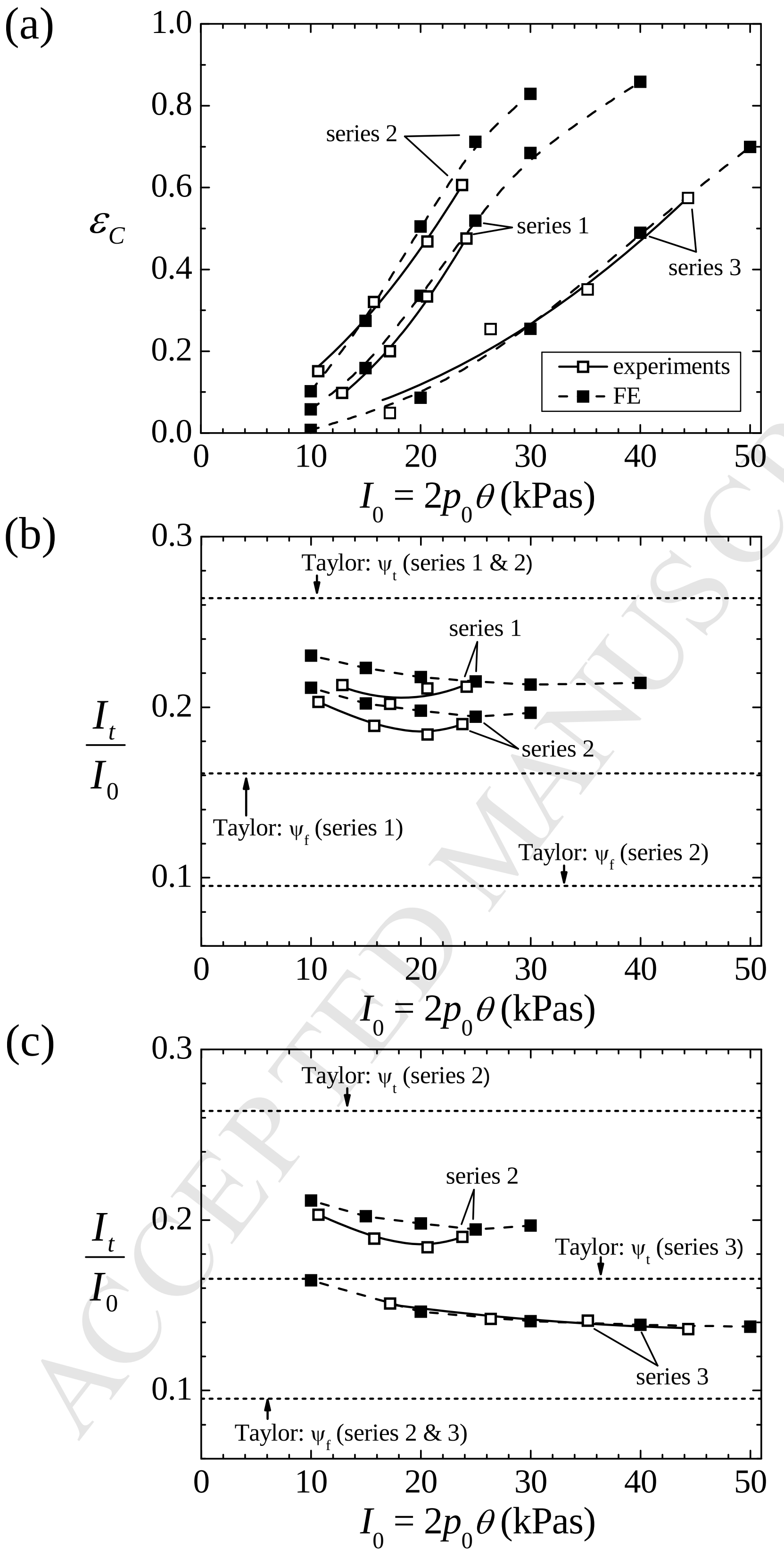
(a)
1.0
0.8
0.6
0.4
0.2
0.0
ε_C
series 2
series 1
series 3
experiments
FE
0
10
20
30
40
50
$I_0 = 2p_0\theta$ (kPas)
(b)
0.3
0.2
0.1
$\frac{I_t}{I_0}$
Taylor: ψ_t (series 1 & 2)
series 1
series 2
Taylor: ψ_f (series 1)
Taylor: ψ_f (series 2)
0
10
20
30
40
50
$I_0 = 2p_0\theta$ (kPas)
(c)
0.3
0.2
0.1
$\frac{I_t}{I_0}$
Taylor: ψ_t (series 2)
series 2
Taylor: ψ_t (series 3)
series 3
Taylor: ψ_f (series 2 & 3)
0
10
20
30
40
50
$I_0 = 2p_0\theta$ (kPas)

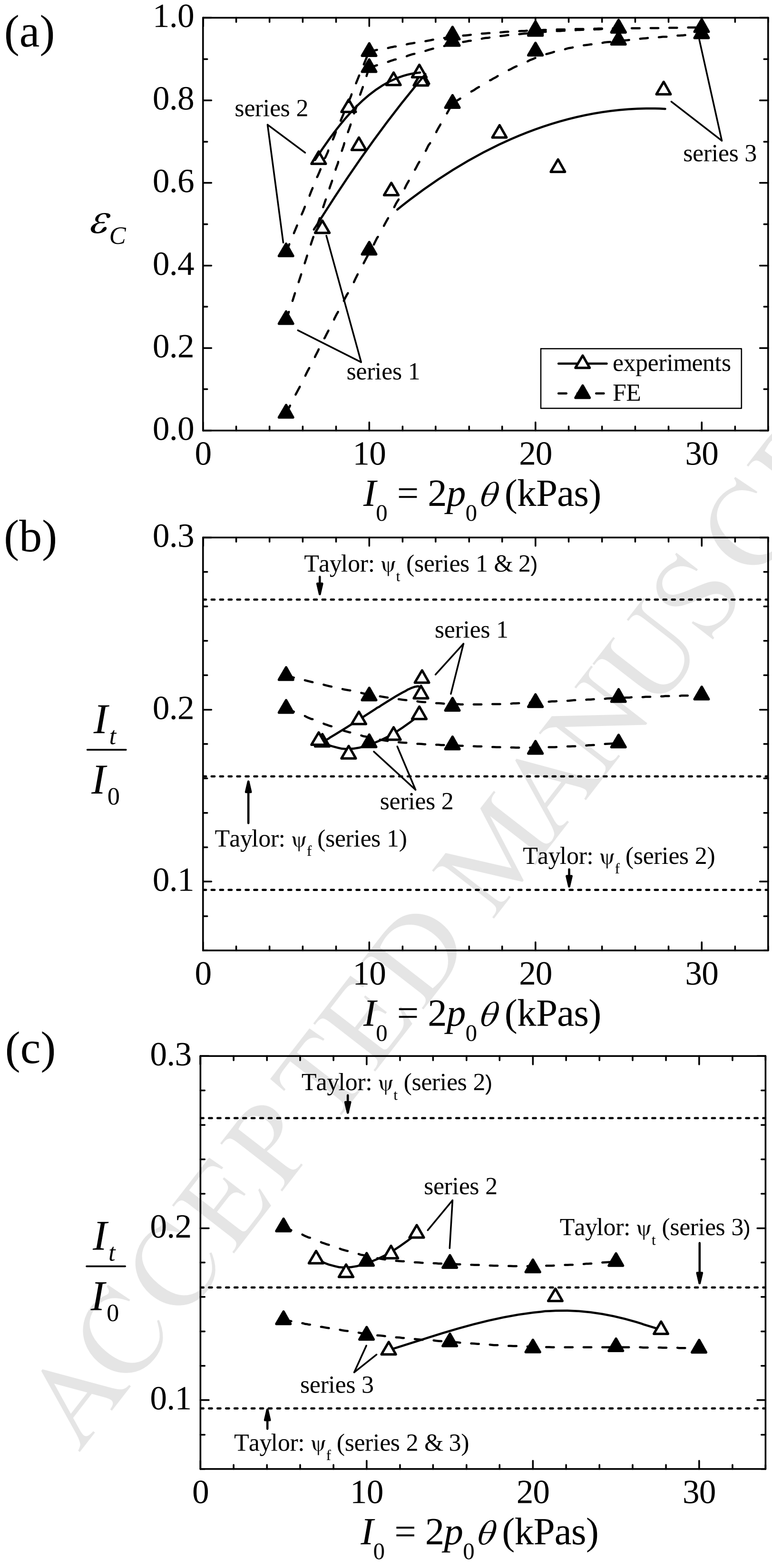
(a)
ε_C
1.0
0.8
0.6
0.4
0.2
0.0
series 2
series 3
series 1
experiments
FE
0
10
20
30
$I_0 = 2p_0\theta$ (kPas)
(b)
0.3
0.2
0.1
$\frac{I_t}{I_0}$
Taylor: ψ_t (series 1 & 2)
series 1
series 2
Taylor: ψ_f (series 1)
Taylor: ψ_f (series 2)
0
10
20
30
$I_0 = 2p_0\theta$ (kPas)
(c)
0.3
0.2
0.1
$\frac{I_t}{I_0}$
Taylor: ψ_t (series 2)
series 2
Taylor: ψ_t (series 3)
series 3
Taylor: ψ_f (series 2 & 3)
0
10
20
30
$I_0 = 2p_0\theta$ (kPas)